Electronic Supplementary Material (ESI) for Nanoscale.
This journal is © The Royal Society of Chemistry 2019

SUPPLEMENTARY INFORMATION FOR

Mapping the Dielectric Constant of a Single Bacterial Cell at the Nanoscale with Scanning Dielectric Force Volume Microscopy

Martí Checa,[1,2] Ruben Millan-Solsona,[1,2] Nuria Blanco-Cabra,[3] Eduard Torrents,[3] Rene Fabregas,[1] Gabriel Gomila[,1,2]*

[1]Nanoscale Bioelectrical Cahracterization, Institut de Bioenginyeria de Catalunya (IBEC), The Barcelona Institute of Science and Technology, c/ Baldiri i Reixac 11-15, 08028, Barcelona, Spain

[2]Departament d'Enginyeria Electrònica i Biomèdica, Universitat de Barcelona, C/ Martí i Franquès 1, 08028, Barcelona, Spain

[3]Bacterial Infections: Antimicrobial Therapies, Institut de Bioenginyeria de Catalunya (IBEC), The Barcelona Institute of Science and Technology, c/ Baldiri i Reixac 11-15, 08028, Barcelona, Spain

*ggomila@ibecbarcelona.eu

S1. Force components in Electrostatic Force Microscopy and their relation to the cantilever deflection and oscillation amplitude.

In Electrostatic Force Microscopy (EFM) an ac voltage of amplitude v_{ac} and frequency ω_{el}, i.e. $V(t) = v_{ac}\cos(\omega_{el}t)$, is applied between a conductive AFM probe and the sample substrate. The electric force acting on the probe is given by

$$F_{el}(t) = \frac{1}{2}\frac{dC(z)}{dz}\left(V(t) - V_{CP}\right)^2; \qquad \text{(S1)}$$

where V_{CP} is the contact potential and dC/dz the capacitance gradient. By expanding Eq. (S1) one obtains three components, namely, a "static" DC bending, and two oscillatory components at ω_{el} and $2\omega_{el}$, respectively, given by

$$F_{el,DC} = \frac{1}{2}\frac{dC(z)}{dz}\left(\frac{v_{ac}^2}{2} + V_{CP}{}^2\right); \qquad \text{(S2)}$$

$$F_{el,\omega}(t) = \frac{dC(z)}{dz} v_{ac} V_{CP} \cos\left(\omega_{el} t\right); \qquad \text{(S3)}$$

$$F_{el,2\omega}(t) = \frac{1}{4}\frac{dC(z)}{dz} v_{ac}^2 \cos\left(2\omega_{el} t\right); \qquad \text{(S4)}$$

The electric force is a distributed force acting on the tip and cantilever parts of the probe. Accordingly, the induced deflection and oscillation amplitudes, for frequencies below the mechanical resonance frequency, are given by

$$D_{DC} = \frac{1}{2k}\left(C'_{tip} + \beta C'_{cant}\right)\left(\frac{v_{ac}^2}{2} + V_{CP}^2\right) = D_{DC,tip} + D_{DC,cant} \qquad \text{(S5)}$$

$$A_{\omega} = \frac{1}{k}\left(C'_{tip} + \beta C'_{cant}\right) v_{ac} V_{CP} = A_{\omega,tip} + A_{\omega,cant} \qquad \text{(S6)}$$

$$A_{2\omega} = \frac{1}{4k}\left(C'_{tip} + \beta C'_{cant}\right) v_{ac}^2 = A_{2\omega,tip} + A_{2\omega,cant} \qquad \text{(S7)}$$

where k is the equivalent spring constant and β a factor that depends on the cantilever orientation with respect to the bottom electrode (see Bonaccurso, E.; Schönfeld, F.; Butt, H.-J. Electrostatic

forces acting on tip and cantilever in atomic force microscopy. Phys. Rev. B 2006, 74, 085413). Therefore, the cantilever deflection and the cantilever oscillation amplitude both have two contributions, one due to the electric force acting on the cantilever and one due to the force acting on the tip. In most situations the cantilever contribution can be approximated by a constant and treated as an offset contribution, as we did in the manuscript.

S2. Calibration of EFM data.

Deflection

In the manuscript the deflection is defined with respect to the long-distance baseline value with the voltage applied (and not with respect to the baseline with no applied voltage). Since the long-distance force is basically due to the cantilever contribution, and according to Eq. (S5), the reported deflection corresponds to the deflection induced by the force acting on the tip, $D_{DC,tip}$. The conversion of raw deflection values (in terms of volts measured by the photodiode) to quantitative deflections (in nm) is done as usual:

$$D_{DC,tip}(nm) = \frac{D_{DC,tip}(V)}{m(V/nm)} \qquad \text{(S8)}$$

where $m(V/nm)$ is the photodiode sensitivity (slope of the contact part of the deflection approach curves).

2ω–Oscillation amplitude

The oscillation amplitude values reported in the manuscript are taken in absolute terms (and not referenced to any baseline value). Therefore, they contain both the contribution from the cantilever and from the tip. The conversion of the raw 2ω-oscillation amplitude (in terms of the photodiode-lock-in measured amplitude in volts) to a calibrated oscillation amplitude (in terms of nanometres) is done as usual,

$$A_{2\omega}(nm) = \frac{A_{2\omega}(V) - A_{2\omega,offset}(V)}{m(V/nm)\,G_{lock-in}(V/V)} \qquad \text{(S10)}$$

where $G_{lock-in}(V/V)$ and $A_{2\omega,offset}(V)$ are the lock-in gain and offset, respectively. Here, we assumed the applied frequency is well below half the mechanical resonance frequency of the probe. According to Eqs. (S7) and (S10) the "total" capacitance gradient is then given by

$$C^{'}\left(aF/nm\right)=C_{tip}^{'}\left(aF/nm\right)+\beta C_{cant}^{'}\left(aF/nm\right)=\frac{4k\left(nN/nm\right)\left(A_{2\omega}\left(V\right)-A_{2\omega,offset}\left(V\right)\right)}{m\left(V/nm\right)G_{lock-in}\left(V/V\right)v_{ac}^{2}\left(V\right)} \qquad \text{(S11)}$$

The cantilever contribution to the capacitance gradient is nearly constant, and hence it can be treated as an offset, as we did in the manuscript.

S3. Time and frequency dependence of the electric forces in Electrostatic Force Microscopy.

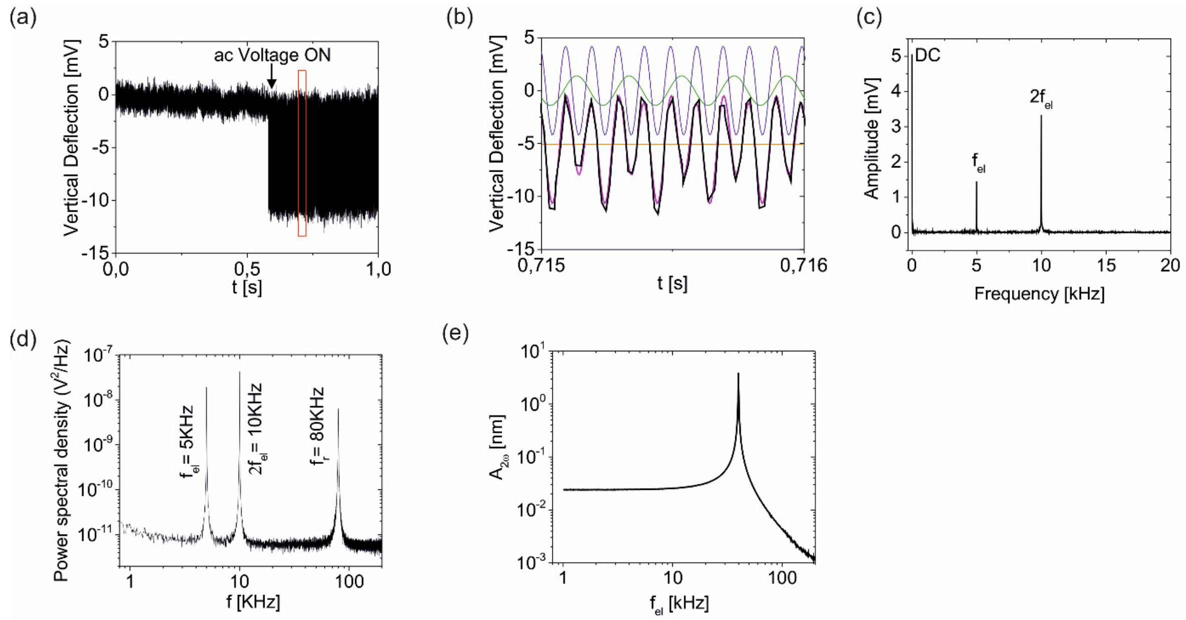

Figure S1. (a) Time response of the vertical deflection of one of the probes used in the manuscript when an ac voltage of frequency f_{el}= 5 kHz and amplitude 3 V is applied. (b) (black line) Zoom in of the time response of the vertical deflection around the red square area marked in (a). (pink line) Fit of the experimental time response of the vertical deflection with the theoretical time response predicted by Eq. (S1). (orange, green and blue lines) Decomposition of the time response of the vertical deflection into the DC, ω_{el} and $2\omega_{el}$ components, respectively. (c) Fourier transform of the vertical deflection time response shown in (b). Three peaks appear, which correspond to the DC, ω_{el} and $2\omega_{el}$ components, whose amplitude matches with those of the components shown in (b). (d) Thermal noise spectra of another of the probes used in the manuscript, with an ac voltage applied of frequency f_{el}=5 kHz and amplitude 3 V. The three peaks correspond, respectively, to the ω_{el} and $2\omega_{el}$ harmonics of the applied voltage at f_{el}=5 kHz and $2f_{el}$=10 kHz, and the first mechanical resonance mode of the probe (f_r~80 kHz). (e) Dependence of the $2\omega_{el}$-oscillation

amplitude with the frequency of the electric voltage applied. A peak appears at $f_{el}=f_r/2=40$ kHz. SDFVM data in the main text are taken at $2f_{el}=10$ kHz, well within the flat part of the frequency response spectra. Parameters: lock-in gain, $G=200$, photodiode sensitivity, $m=40$ mV/nm, equivalent spring constant $k=1.7$ N/m.

S4. Building up topographic and EFM images from EFM sets of data.

The ensemble of 128x128 raw vertical deflection and 2ω-oscillation amplitude approach curves of the EFM set of data corresponding to Fig. S3 below is shown in Fig. S2a and S2b, respectively. From them, the topographic and EFM images in the different imaging modes can be obtained following the procedure schematically shown in Fig. S2c and S2d.

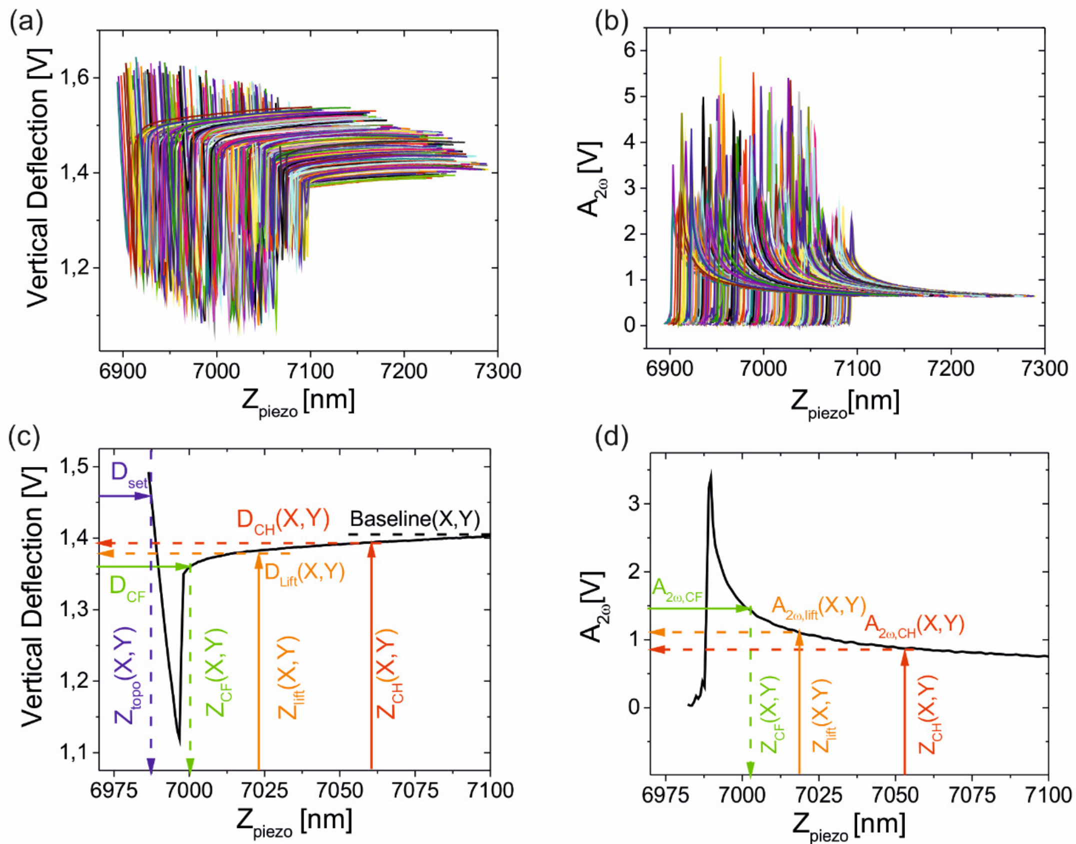

Figure S2. Ensemble of the N=128x128 raw approach curves for (a) the vertical deflection and (b) the 2ω–oscillation amplitude for the EFM set of data corresponding to Fig. S3 below. (c) and (d) Schematic definition of the main parameters used to extract the topographic and EFM images from the EFM set of approach curves. We include the possibility to built up also dc EFM images (not considered in the manuscript) from the non-contact part of the vertical deflection approach curve in (c).

S4.1. Topographic images

The topographic images are obtained from the vertical deflection curves (Fig. S2a) by setting a positive (or null) deflection set-point at each curve with respect to the long distance baseline, $D_{set} \geq 0$, and retrieving the corresponding Z piezo displacement values, $Z_{topo}(X,Y;D_{set})$ (Fig. S2c blue lines). Figure S3a shows a topographic image obtained from the deflection approach curves in Fig. S2a, once callibrated, by setting a set point $D_{set} = 0\ nm$. To correct for sample tilting, sample vertical drift, piezo scanner curvature, etc. the raw image is flatted using a conventional SPM processing software. The resulting flattened topographic image is the result of subtracting a surface $Z_{flatten}(X,Y)$ to the raw topographic image, i.e. $Z_{topo,flatten}(X,Y) = Z_{topo}(X,Y) - Z_{flatten}(X,Y)$. The flattened topographic image corresponding to Fig. S3a is shown in Fig. S3b, while the subtracted flattening surface is shown in Fig. S3c. The deflection set-point to obtain the topographic image is defined with respect to the baseline of each curve (and not with respect to an absolute value). In this way, one corrects for the effects of laser spot drifting on the photodiode (which is evidenced by the vertical shift of the vertical deflection approach curves in Fig. S2a). Figure S3d shows an image of the baseline values extracted, where the drifting of laser spot is made evident. The baseline values of the vertical deflection curves include, in the case of EFM, the long-distance electrostatic DC bending of the cantilever associated to the applied ac potential (see Sec. S1). At long enough distances, it is expected that the DC bending becomes independent from the local dielectric and topographic properties of the sample, as it is shown in Fig. S3d.

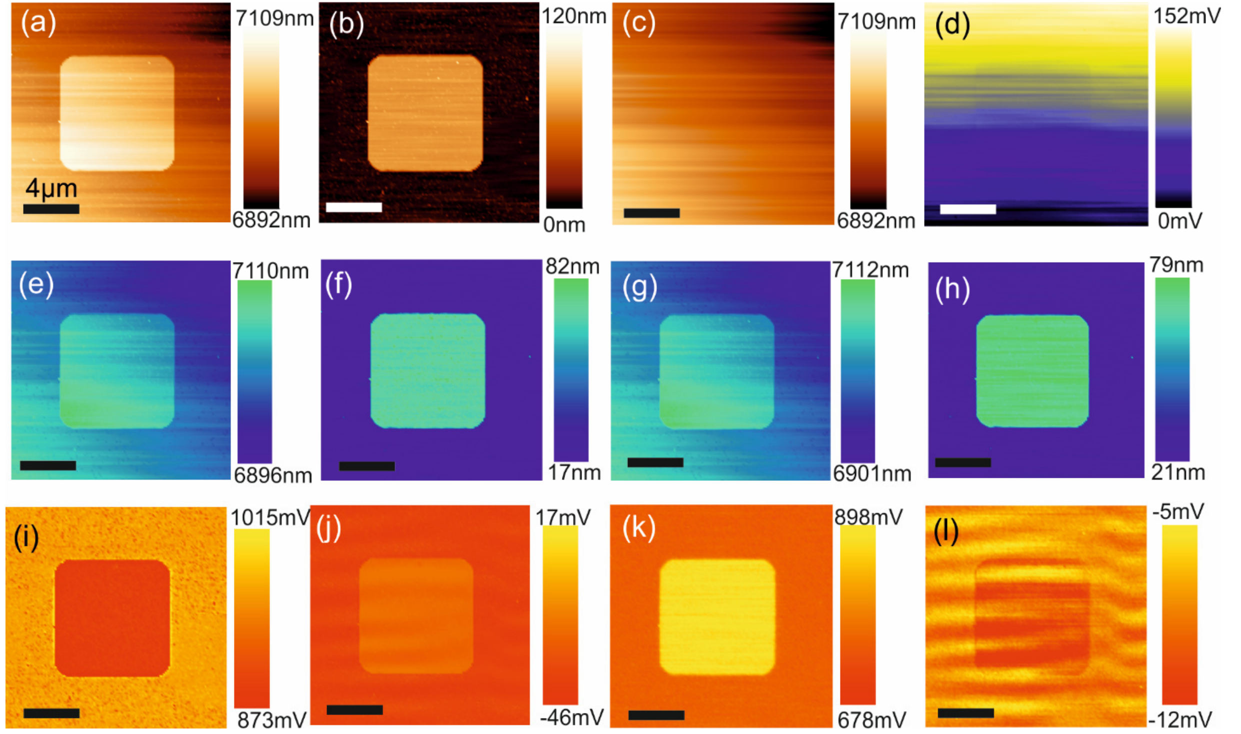

Figure S3. (a) Raw and (b) flattened topographic images at set point D_{set}=0 nm (with respect to the baseline value) obtained from the raw deflection EFM approach curves in Fig. S2. (c) "Plane" subtracted to the raw topographic image in (a) to flatten it and obtain (b). (d) Baseline values calculated as the average of the furthest 30 nm of the vertical deflection curves as a function of position on the sample. (e) Raw and (f) flattened constant DC force EFM images at set point D_{CF}=−0.05 V, corresponding to a force of ~2.1 nN. (g) Raw and (h) flattened constant ac force EFM images at set point $A_{2\omega,CF}$=1.5 V, corresponding to a force of ~0.22 nN. (i) ac and (j) DC lift mode EFM images at a lift distances of 50 nm and 20 nm, respectively. (k) ac and (l) DC constant height EFM images at a substrate distance of 120 nm. Experimental parameters: Z_{length}=200 nm, time per pixel 150 ms, v_{ac}=3V, f_{el}=5 kHz, HQ-NSC19/Cr-Au probes, equivalent spring constant k=1.7 N/m. Scalebar in X is 4μm.

S4.2. Constant electric force EFM images

From the set of approach curves of the vertical deflection and 2ω-oscillation amplitude in Figs. S2a and S2b, respectively, we can obtain EFM images at constant electric force by either setting a negative set-point to the vertical deflection approach curves, $D_{set}<0$, and retrieving the corresponding Z-piezo displacement values, $Z_{CF\text{-}DC}(X,Y;D_{set})$, or by setting a set-point, $A_{2\omega,set}$, to the 2ω-oscillation amplitude approach curves and retrieving the corresponding piezo displacement values $Z_{CF\text{-}2\omega}(X,Y; A_{2\omega,set})$ (green lines in Fig. S2c and S2d, respectively). Examples of images obtained in this way are shown in Figs. S3e and S3g, respectively. These images, like the topographic image, are affected by the vertical drift and sample tilting. We subtract these effects by subtracting the same flattening surface subtracted to the raw topographic image, i.e. $Z_{CF-DC,flatten}(X,Y) = Z_{CF-DC}(X,Y) - Z_{flatten}(X,Y)$ and $Z_{CF-2\omega flatten}(X,Y) = Z_{CF-2\omega}(X,Y) - Z_{flatten}(X,Y)$. The corresponding flattened images are shown in Figs. S3f and S3h. Note that the set-point $A_{2\omega,set}$ is defined in absolute terms (and not with respect to a baseline value) since the oscillation amplitude is not affected by laser spot drifting effects, as it can be observed in Fig. S2b.

S4.3. Lift mode EFM images

Lift-mode EFM images are obtained by selecting Z piezo values equal to the piezo value corresponding to the topography lifted by a constant amount, i.e. $Z_{lift}(X,Y) = Z_{topo}(X,Y) + Z_{lift}$ and then determining the values of either the vertical deflection $D_{lift}(X,Y;Z_{lift})$, to obtain the DC lift mode EFM image, or the 2ω-oscillation amplitude, $A_{2\omega,lift}(X,Y,Z_{lift})$, to obtain the 2ω-lift mode EFM image (orange lines in Fig. S2c and S2d, respectively). Examples of images obtained in this

way from the approach curves shown in Fig. S2a and S2b are shown in Figs. S3i and S3j, respectively. Note that in this case no flattening must be applied.

S4.4. Constant height EFM images

Constant height EFM images are obtained by setting the Z piezo values over a surface that represents a surface parallel to the substrate of the sample (and to the flattening surface) at a given position (X_0,Y_0), i.e. $Z_{CH}(X,Y) = Z_{flatten}(X,Y) + Z_{CH}$, and then determining the corresponding values of either the vertical deflection $D_{CH}(X,Y,Z_{CH})$, to obtain the DC constant height image, or the 2ω-amplitude, $A_{2\omega,DC}(X,Y,Z_{CH})$, to obtain the 2ω-constant height image (red lines in Fig. S2c and S2d, respectively). Examples of images obtained in this way are shown in Figs. S3k and S3l, respectively.

S5. Building up topographic and EFM images from surface cuts of the EFM cubes of data.

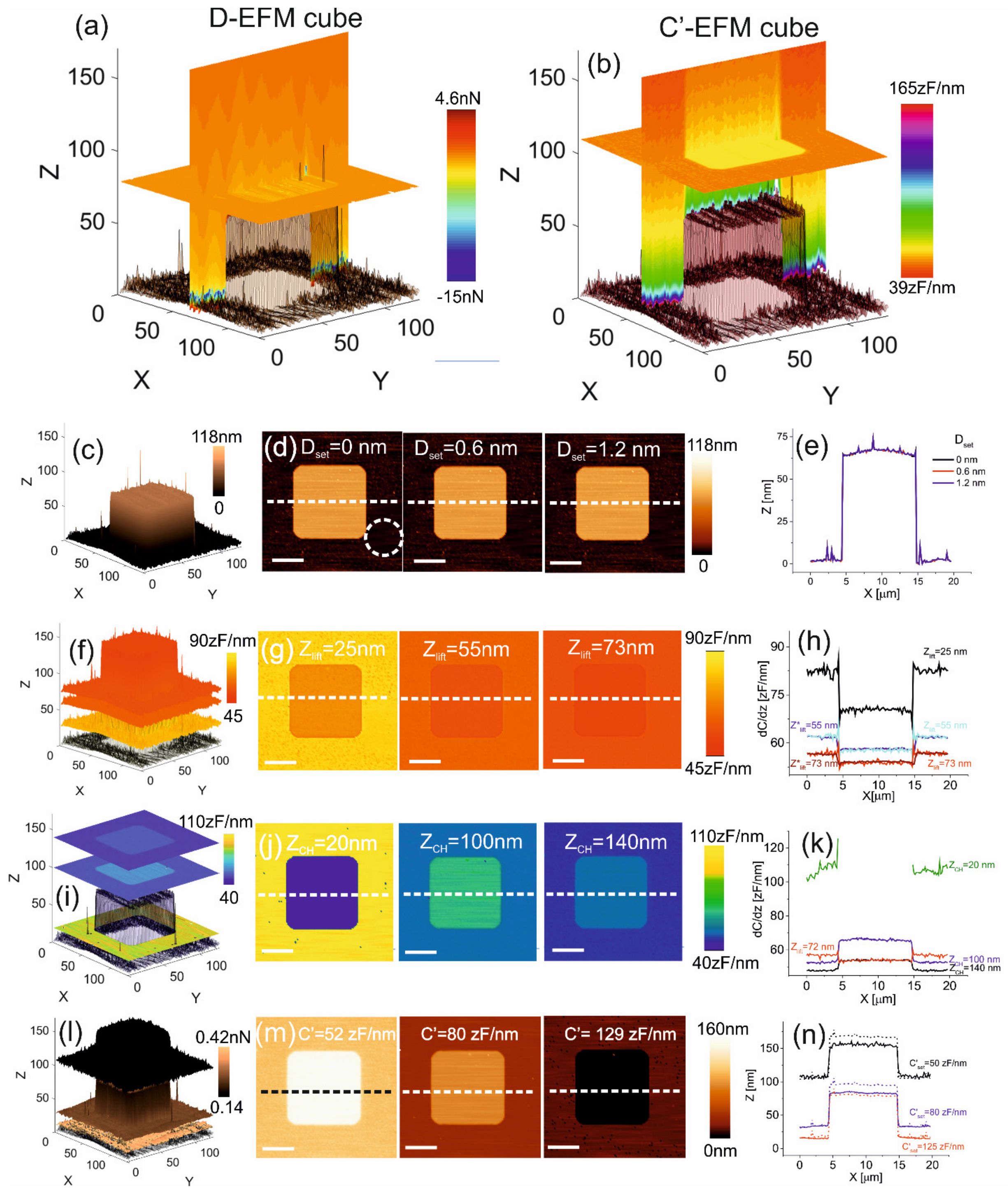

Figure S4. (a) Deflection and (b) capacitance gradient (2ω–oscillation amplitude) EFM cubes of data for a silicon dioxide pillar ~60 nm thick and ~10 μm wide micropatterned on a highly doped

silicon substrate. Each cube of data contains 128x128x300 voxels. The range and duration of each curves is 200 nm and 150 ms, respectively. The ac applied voltage has amplitude 3 V and frequency 5 kHz. The probe is a HQ:NSC/Cr-Au probe with equivalent spring constant k~1.7 N/m, resonance frequency 80 kHz. (c) Deflection EFM cube of data with three (indistinguishable) iso-deflection surfaces at deflection set-points D_{set}=0 nm, 0.6 nm and 1.2 nm. (d) Corresponding topographic images obtained from the cuts in (c). The dashed circle represents a clean region of the substrate. (e) (continuous lines) Topographic cross-section profiles along the dashed lines in the images in (d). The dashed line represents a topographic cross-section profile obtained with 0 V applied. (f) Capacitance gradient EFM cube of data with three surfaces representing the sample topography lifted at distances Z_{lift}=25 nm, 55 nm and 73 nm, and (g) corresponding obtained lift-mode EFM images. (h) (Black, dark blue and red lines) Corresponding capacitance gradient cross-section profiles along the dashed lines in (g). (light blue and magenta lines) Capacitance cross-section profiles for an image directly acquired in conventional two-pass lift mode at Z_{lift}=55 nm and 73 nm, respectively. (i) Capacitance gradient EFM cube of data with three surfaces representing constant height planes at distances Z_{CH}= 25 nm, 100 nm and 140 nm and (j) corresponding obtained constant height EFM images. At Z_{CH}=25 nm regions of the sample lower than the constant height distance, and for which no data are available, are shown in black color. (k) (Black, dark blue and green lines) Corresponding capacitance gradient cross-section profiles along the dashed lines in (g). (l) Capacitance gradient EFVM cube of data with three iso-capacitance gradient (iso-force) surfaces at values dC/dz_{set}= 52 zF/nm, 80 zF/n, 129 zF/nm and (m) corresponding obtained constant capacitance gradient (electric force) EFM images. (n) (thick lines) Constant capacitance gradient height cross-section profiles along the lines in (m). The thin lines represent the lifted topographic profiles. X-scalebar in the images is 4 μm.

S6. Additional data on tip geometry calibration

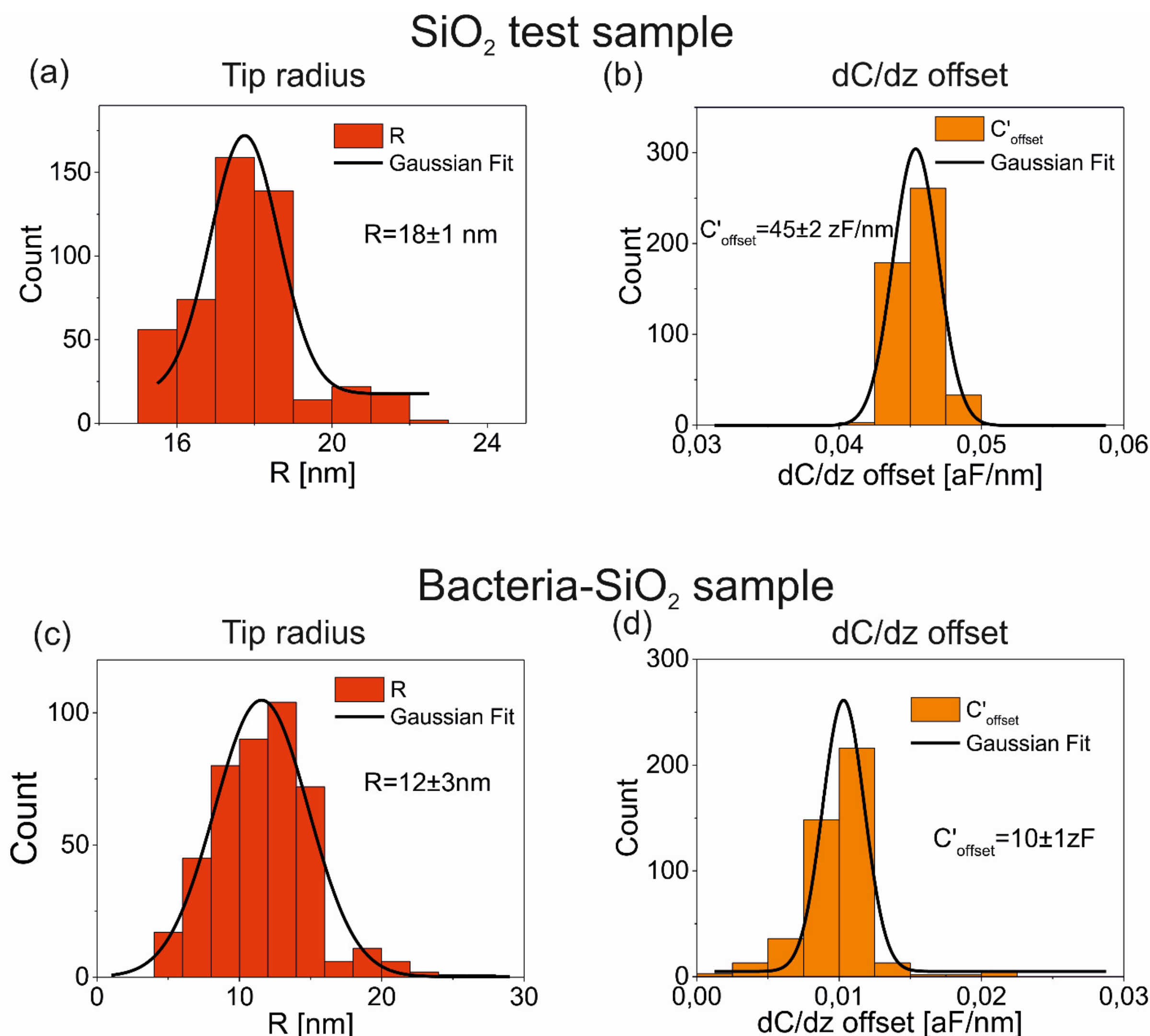

Figure S5. (a) and (b) Statistical distribution of the radii and capacitance gradient offsets obtained by calibrating the tip geometry in the 21x21 area inside the highlighted dashed circle in Fig. S4d. From a Gaussian fit of the data we obtain the mean values R=18 ± 1 nm, θ=14° and C'_{offset}= 45 ± 2 zF/nm reported in the manuscript. (c) and (d) Idem for Fig. 2 of the manuscript, obtaining R=12 ± 3 nm, θ=5° and C'_{offset}= 10 ± 1 zF/nm. The remaining tip parameters are set to their nominal values, i.e. H=12.5 µm, W=3 µm, L=3 µm.

S7. EFM data cubes for the sample in Fig. 2

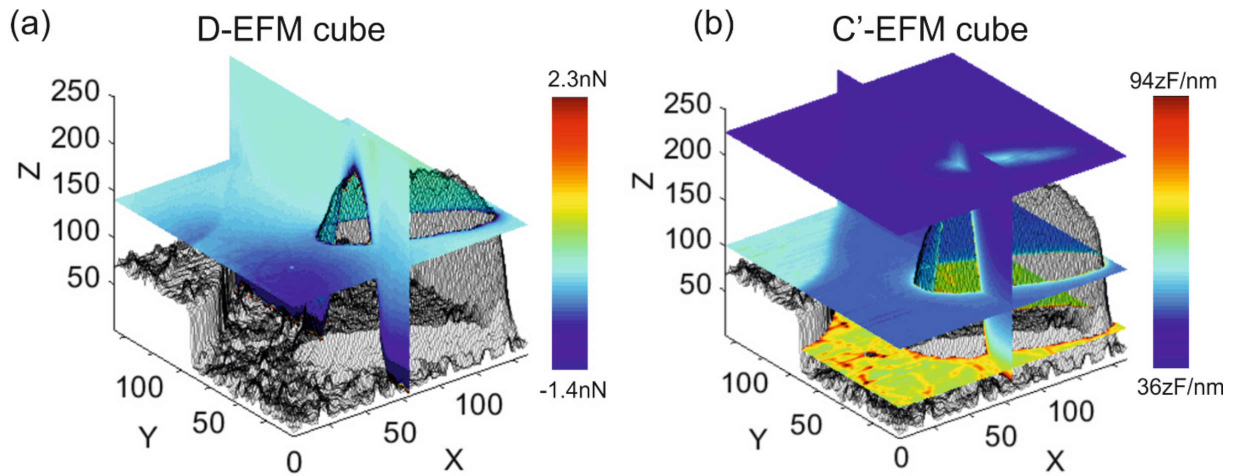

Figure S6. (a) Deflection and (b) capacitance gradient (2ω–oscillation amplitude) EFM cubes of data corresponding to Fig. 2 of the manuscript. Each cube of data contains 128x128x300 voxels. Experimental parameters: range and duration of each curve 250 nm and 120 ms; ac applied voltage amplitude and frequency 4 V and 5 kHz; HQ:NSC/Cr-Au probe with equivalent spring constant k=1.2 N/m and resonance frequency 66 kHz. See also Video S1 for an animation of the C'-EFM cube.

S8. Additional EFM images of bacterial cells.

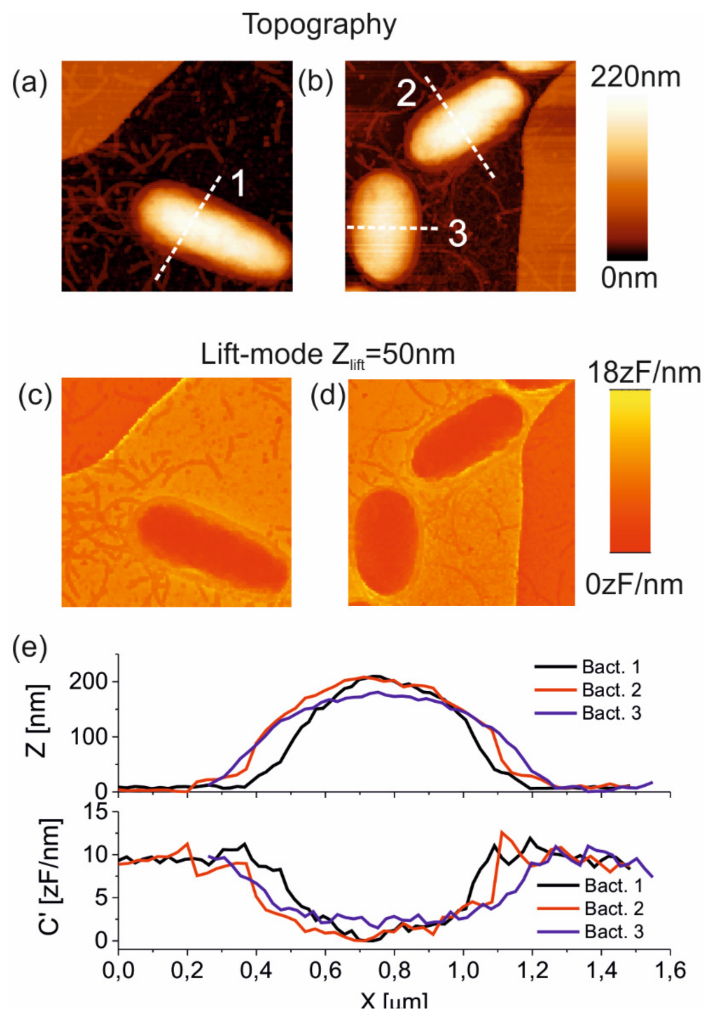

Figure S7. Comparison of the topographic and lift mode EFM images between different bacterial cells on the same sample. (a) and (c) correspond to the bacteria discussed in the main text. (b) and (d) correspond to two additional bacterial cells. Both the topography and the electric response is similar.

S9. Dynamic local geometric models.

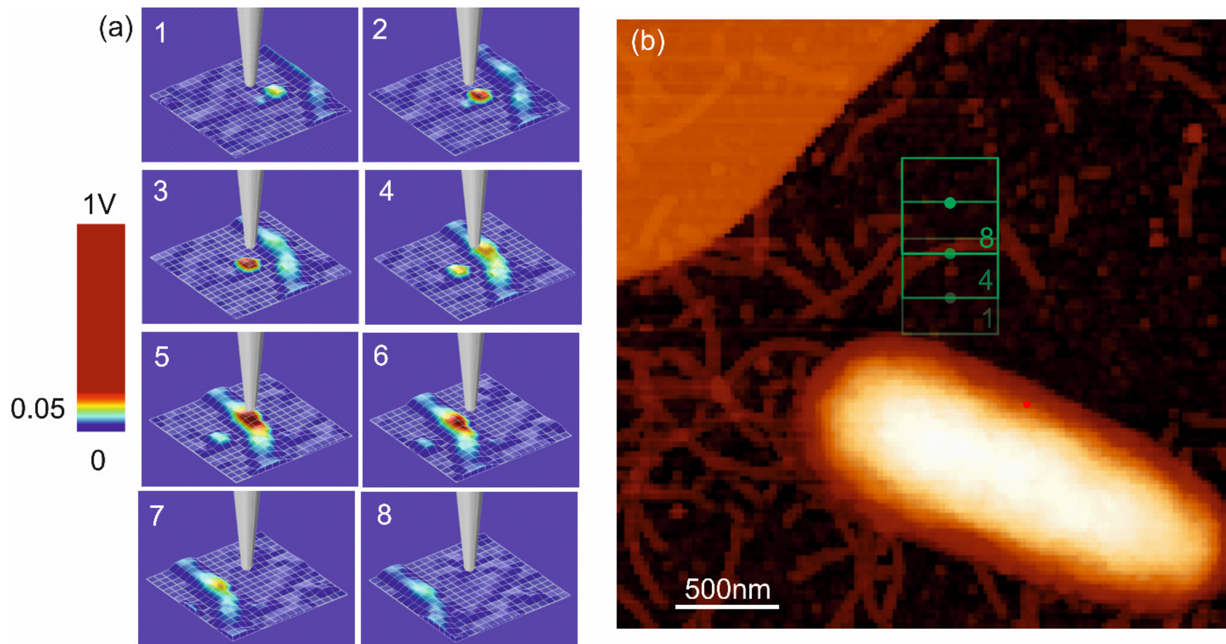

Figure S8. (a) Examples of dynamic reconstruction of the local geometry corresponding to a vertical line along the range of pixels (72,71) (1) to (72,86) (8) in the AFM topographic image shown in (b). The green squares show different positions of the tip and of the area included in the local topographic models. Video S2 shows an animated version of the images shown in (a).

S10. Tip deconvolution corrected dielectric constant distribution for the bacterial flagella

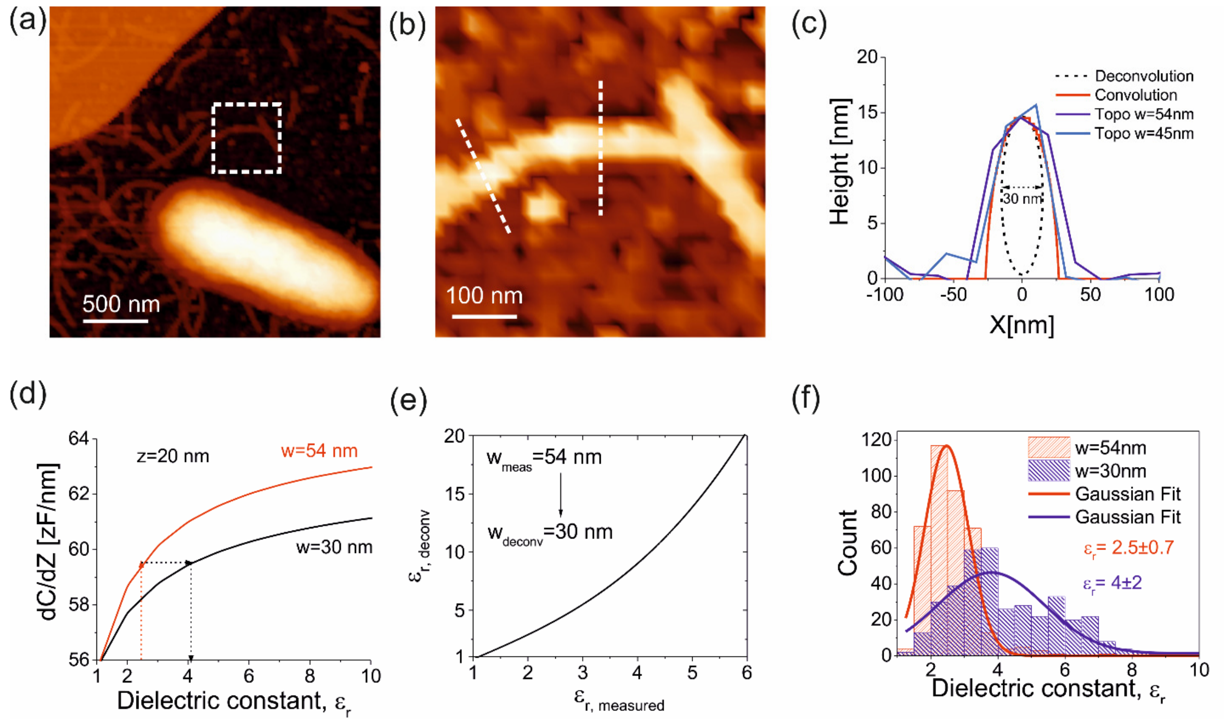

Figure S9. (a) Topographic image of the sample analysed with a highlighted region used for the tip convolution analysis. (b) Digital zoom-in of the topographic image in the region highlighted in (a). (c) (blue lines) Cross-section topographic profile along the dashed lines in (b); (red line) calculated tip-convoluted profile, giving a deconvoluted width w_{deconv}=30 nm; (dashed line) deconvoluted cross-section of the flagellum. (d) Numerically calculated capacitance gradient for a tip at a distance z=20 nm from a cylindrical wire of height h=15 nm, length l= 1 µm and widths w=54 nm and 30 nm. The dashed line arrows indicate how the conversion of the measured dielectric constant into tip-deconvoluted dielectric constants is performed. (e) Relation between the deconvoluted dielectric constant values and the measured ones. (f) Distribution of tip deconvoluted dielectric constant values (blue bars) and of measured dielectric constant values (red bars). The continuous lines represent Gaussian fits to the distributions giving $\varepsilon_{r,meas}$=2.5±0.7 and $\varepsilon_{r,deconv}$=4±2, as reported in the manuscript.

S11. Limitations of thin film dielectric models applied to heterogeneous topographically complex samples

Figures S9a and S9b show the dielectric constant maps that would be obtained by using analytical and numerical thin film models, respectively, applied to the measurements reported in Fig. 2 (for details on the models see Gomila, G; Gramse, G, Fumagalli, L. Finite-size effects and analytical modeling of electrostatic force microscopy applied to dielectric films. *Nanotechnology* 25, 255702 (2014)). The first aspect to highlight is that at the edges of the micro/nanostructures the dielectric constant values provided by the thin film models are not correct. This fact is observed in the statistical distribution of dielectric constant values for the SiO_2 part of the sample (Fig. 9c), which shows two peaks, corresponding, respectively, to the edge and bulk part of the thin film pillar, instead of a single peak as we obtained with the realistic model used in the manuscript (black bars). This artifact is due to the relevance of lateral forces at the edges, which are not included in the thin film models, and which are compensated by increasing (or decreasing) the value of the local dielectric constant, depending on the tip position with respect to the edge. In some cases, the lateral force effects are so strong that there is no possible value of the dielectric constant able to mimic these effects, which constitutes a clear signature of the limited applicability of thin film models. By contrast, the quantification approach followed in the manuscript, by using the actual sample geometry naturally includes the lateral force effects, and hence provides well defined dielectric constant values at the edges of the micro/nanostructures (see Fig. 3g-3i).

Concerning the values of the dielectric constant obtained on the bulk part of the SiO_2 pillar, the numerical thin film model provides similar values to SDFVM, as expected. Instead, the analytical thin film model tends to provide larger values, since this model is not accurate for thin films with thicknesses larger than the tip radius, as in the present case.

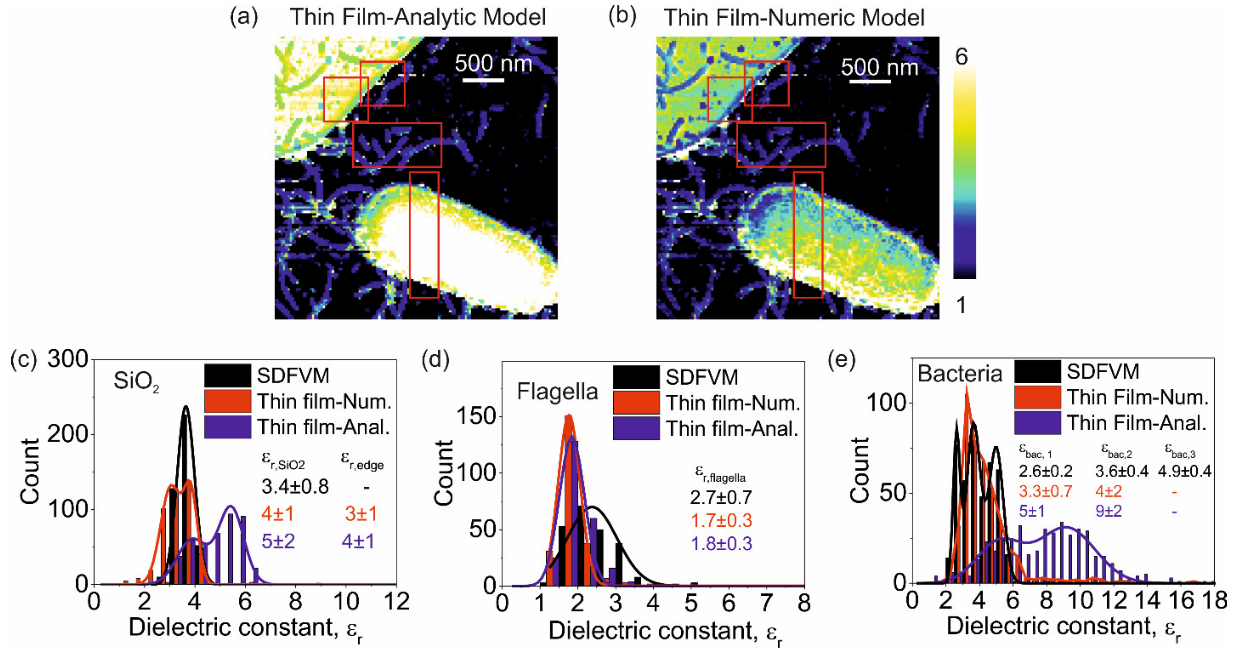

Figure S10. Dielectric constant maps obtained by applying (a) analytical and (b) computational local thin film theoretical models to quantify the C'-EFM cube of data obtained on the sample of Fig. 2. The square and rectangular highlighted regions correspond to the areas statistically analyzed and compared with the predictions of the manuscript. (c)-(e) (red and blue bars) Histogram analysis of the dielectric constant values corresponding to the highlighted regions in (a) and (b), respectively. The black bars correspond to the data obtained with the method of the present work and reported in Fig. 3. The continuous lines represent Gaussian (or double Gaussian) fits to the data. The mean values obtained in each case are show in the figures.

For the bacterial flagella, the dielectric constant values provided by the thin film models (Fig. S9d) tend to be smaller than the values obtained with the model based on the measured topography. This result, which has been already highlighted in the past, is because the thin film models provide the electric polarization force corresponding to an extended thin film of thickness equal to the local height of the nanoscale object. As a result, for small objects the thin film models consider larger

areas and hence predict higher forces, what is compensated by providing smaller dielectric constants. In some cases, again, no value can be found to mimic this effect, showing again the limited applicability of the thin film models. Finally, in the case of the bacterium cell the distribution of dielectric constant values predicted by the analytical thin film model are very far from the distribution obtained with a realistic geometrical model, while the predictions of the numerical thin film model are closer, but they fail to identify the three different contributions that we have identified and discussed in the manuscript (Fig. S9e), again due to the relevance of the lateral force effects on topographically complex samples. Again, in several pixels, no dielectric constant value can be obtained with these models. We then conclude that thin film dielectric models do not provide realistic quantitative dielectric constant values when applied to bacterial cells, or provide values that are affected by the topography of the sample, and hence, they cannot be used to infer information on the sub-cellular bacterial cell composition.

S12. Photodiode sensitivity from EFM sets of data

Among the different parameters needed to calibrate the EFM data, there is the photodiode sensitivity. The photodiode sensitivity is calculated from each vertical deflection approach curve by determining the slope of the contact part of the curves, as usual (see Fig. S10a). Note that since the approach curves are relatively short in SDFVM (to reduce the number of acquired points and hence the image acquisition time) both positive and negative deflection values can be considered in the least square fitting for a better statistical fit and reach good regression coefficients (e.g. $R>0.9$). Figures S10b and S10c show examples of maps of the photodiode sensitivity obtained from SDFVM measurements on a freshly cleaved HOPG substrate and on the sample analyzed in Fig. S2d. Figures S10d and S10e show the corresponding statistical distribution analysis of the respective measured photodiode sensitivities. We observe that for the case of the HOPG the photodiode sensitivity shows a Gaussian distribution with mean value $m=39 \pm 7$ *mV/nm*, while for the case of the SiO_2 micropatterned pillar it is better represented by a double Gaussian distribution with means $m=40 \pm 3$ mV/nm and $m=36 \pm 7$ mV/nm. The sharp Gaussian distribution represents approach curves on "clean" parts of the substrate, while the broader Gaussian distribution represents approach curves on "non-clean" parts of the sample, and hence represents both the photodiode sensitivity and the mechanical deformation of the residues. To reduce the uncertainty in the calibrated SDFVM data associated to the uncertainty in the photodiode sensitivity, which is relatively large, we used a single photodiode sensitivity for the whole set of curves, with a value corresponding to the mean value of the Gaussian distribution of the "clean" parts of the substrate.

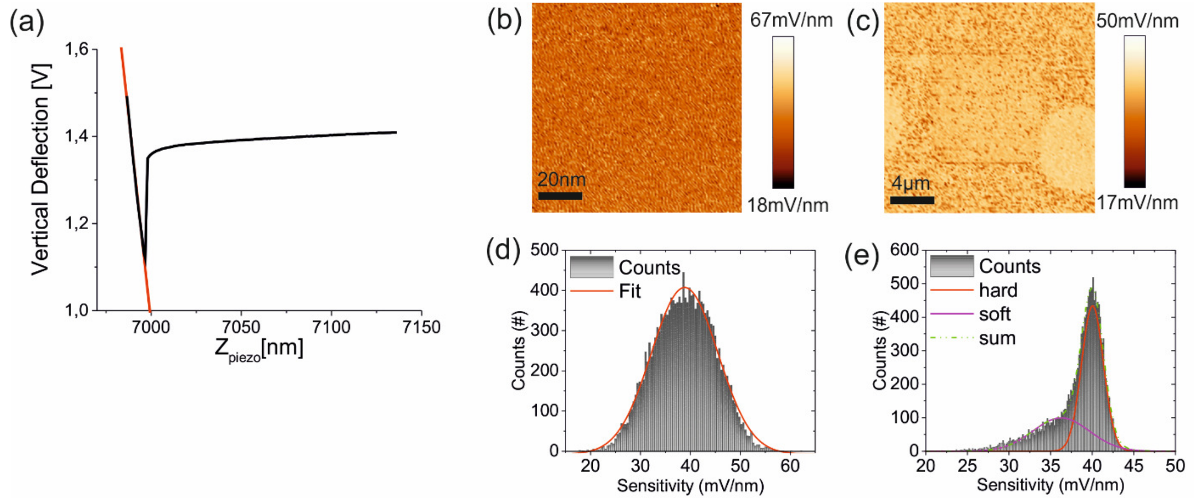

Figure S11. (a) Extraction of the photodiode sensitivity from a vertical deflection EFM approach curve. (b) 128x128 map of the photodiode sensitivity obtained on a freshly cleaved HOPG. (c) Idem for the case of the curves and sample in Figs. S4. (d) Statistical distribution of the photodiode sensitivity obtained from (b). Results show a Gaussian distribution with mean *m*=39 ±7 mV/nm. (e) Idem obtained from (c). In this case, the distribution is fitted with a double Gaussian distribution with *m*=40 ±3 mV/nm and *m*=36 ±7 mV/nm. Experimental parameters: Z_{length}=200 nm, time per pixel 150 ms, v_{ac}=3V, f_{el}=5 kHz, HQ-NSC19/Cr-Au probes, equivalent spring constant *k*=1.28 N/m.

S13. Figure captions Videos

Video S1. Capacitance gradient EFM cube of data (C'-EFM) from which the EFM images displayed in Fig. 2 have been obtained. The video shows the cube of data being cut by different horizontal and vertical planes.

Video S2. Animation of the motion of the tip with respect to the flagella in the numerical calculations (and calculated surface electric potential distribution) corresponding to Fig. S7.